Optics Communications 282 (2009) 1265–1273

Contents lists available at ScienceDirect

Optics Communications

journal homepage: www.elsevier.com/locate/optcom

# A goniometric light scattering instrument with high-resolution imaging

Michel Lequime *, Myriam Zerrad, Carole Deumié, Claude Amra

*Institut FRESNEL, UMR CNRS 6133, Université Paul Cézanne – Ecole Centrale Marseille – Université de Provence Domaine Universitaire de Saint – Jérome, 13397 Marseille, Cedex 20, France*

A R T I C L E I N F O

*Article history:*
Received 17 July 2008
Received in revised form 16 December 2008
Accepted 17 December 2008

*Keywords:*
Scattering measurements
Surface roughness

A B S T R A C T

This paper describes a new goniometric optical scattering instrument whose distinctive features include a mobile light source, a telecentric objective, and a fixed photodiode array. A scientific-grade CCD detector allows the instrument to reliably detect BRDF levels as low as $5 \times 10^{-8}$ $sr^{-1}$, while generating a high-resolution map of light scattered from the sample surface. These data reveal the position and size of localized defects, which can then be excised from the sample to give an unbiased determination of the surface's intrinsic roughness. High-quality signature and calibration data are also obtained, as well as a practical characterization of a silicon wafer.

© 2008 Elsevier B.V. All rights reserved.

## 1. Introduction

The Bidirectional Reflectance Distribution Function (BRDF) is widely used to quantify the roughness of optical surfaces with very high sensitivity [1,2]. This measurement requires illuminating the sample with a light beam at fixed incidence and recording the angular distribution of scattered light. Typically the detector is mounted on a rotating arm that moves within the plane of incidence, but in some applications light scattered outside this plane is also considered [3–13].

For surfaces of low roughness (i.e., whose irregularities are small compared to the wavelength of the beam), the result of this measurement is directly connected to the power spectral density of the surface profile, i.e. the spatial frequency spectrum of its roughness measured in inverse length units. The root-mean-square (rms) roughness of the surface is obtained by integrating this power spectral density over limits defined by the wavelength of the light beam and the angular range of scattered light measurements (see for instance [14]).

However, the results of such roughness measurements can be dramatically modified by a few isolated surface defects under the probe beam [15]. It is possible to characterize each sample beforehand by scanning 100% of its surface with a focused laser beam; by observing scattered light just off the specular direction, any particles or surface defects are very easily detected. The results of this quick mapping can be used to select a representative area for roughness characterization. If the particle or defect density is too high, the substrate will have to be cleaned and perhaps repolished.

In the case of coated samples, the situation is a little different. Their surfaces can include permanent defects [16], either replications of residual substrate defects (sleeks, scratches and digs) or created by the coating process itself (coating voids, inclusions). Such defects cannot be suppressed by further cleaning or polishing. Moreover, if the goal is to optimize a coating process, it is necessary to quantify not just the intrinsic roughness of defect-free areas but also the evolution of sample roughness in the vicinity of defects. Of course, the defect distribution itself (in terms of size and number) is also important.

This paper describes a goniometric light scattering instrument that satisfies these requirements. It is able to record BRDF values as low as $5 \times 10^{-8}$ $sr^{-1}$, while avoiding the contributions of isolated defects. This CCD angle-resolved scattering (CCD-ARS) instrument is ideal for determining the intrinsic scattering properties of coated surfaces.

This paper is organized as follows: Section 2 discusses a numerical simulation of the influence of localized defects on BRDF data, and shows that it is possible to determine their positions and dimensions using our CCD-ARS instrument. Section 3 provides a detailed description of the experimental set-up. Section 4 computes its measurement range and detection limit. Experimental results obtained on a perfect diffuser and a silicon wafer are given in Section 5. A summary of our main achievements and some possible improvements to the instrument can be found in Section 6.

## 2. Numerical simulations and related analysis

### 2.1. Impact of localized defects on the scattering function

To demonstrate the impact of localized defects on scattering, let us consider a low-roughness plane silica surface shaped like a

* Corresponding author. Tel.: +33 49 128 8395; fax: +33 49 128 8067.
*E-mail address:* michel.lequime@fresnel.fr (M. Lequime).

0030-4018/$ - see front matter © 2008 Elsevier B.V. All rights reserved.
doi:10.1016/j.optcom.2008.12.053

square (with side $L = 500\ \mu m$) and illuminated by a collimated beam at wavelength $\lambda$. The refractive index of the incident medium is $n_0$. The surface profile is expressed as an $N \times N$ height array, where $N = 2L/\lambda$. This choice ensures that the numerical simulations take into account surface variations in the adequate spatial frequency range [14].

A realistic surface profile is created using the following mathematical procedure. We start by generating an $N \times N$ matrix of uniformly distributed random numbers between $-\frac{1}{2}$ and $\frac{1}{2}$. Next, we compute the 2D Fast Fourier Transform (FFT) of this array. Finally, we apply the Gaussian/Exponential filter $F$ used in our previous theoretical works [17]:

$$F(\sigma) = \frac{(\delta_g L_g)^2}{4\pi} e^{-(\sigma L_g/2)^2} + \frac{(\delta_e L_e)^2}{2\pi}[1 + (\sigma L_e)^2]^{-3/2}, \quad (1)$$

where $\sigma$ is the spatial pulsation (i.e. the spatial frequency $v$ multiplied by $2\pi$). Finally, a 2D surface profile $h_F(x, y)$ is obtained by computing the inverse FFT of this filtered array.

We can now simulate the effect of this synthetic surface on the incident beam by using the first-order theory (which is well adapted to surfaces of low roughness) and compute the power spectral density of scattered light $J(\sigma_x, \sigma_y)$ by applying the classical formula [17–19]

$$J(\sigma_x, \sigma_y) = C(\sigma_x, \sigma_y) \cdot \gamma(\sigma_x, \sigma_y) \cdot \Phi_0 \quad (2)$$

where $C(\sigma_x, \sigma_y)$ is a term derived from electromagnetic theory, $\Phi_0$ is the optical power of the incident beam, and $\gamma(\sigma_x, \sigma_y)$ is the 2D roughness spectrum of the surface defined by

$$\gamma(\sigma_x, \sigma_y) = \frac{4\pi^2}{L^2} \left|\tilde{h}_F(\sigma_x, \sigma_y)\right|^2. \quad (3)$$

Here $\tilde{h}_F(\sigma_x, \sigma_y)$ is the Fourier Transform of the surface profile. Taking into account the basic relationship between spatial pulsation coordinates $(\sigma_x, \sigma_y)$ and scattering angles $(\theta, \phi)$

$$(\sigma_x, \sigma_y) = \frac{2\pi n_0}{\lambda} \sin\theta \cdot (\cos\phi, \sin\phi) = \sigma \cdot (\cos\phi, \sin\phi) \quad (4)$$

we can compute the intensity of the light scattered by the surface in the plane of incidence (i.e. for $\phi = 0$)

$$I(\theta) = \left(\frac{2\pi n_0}{\lambda}\right)^2 J(\sigma, 0) \cdot \cos\theta \cdot \Phi_0 \quad (5)$$

and, at the end, the scattering function $S$ (or cosine-corrected BRDF) of this synthetic sample

$$S(\theta) = \mathrm{BRDF} \cdot \cos\theta = \frac{I(\theta)}{\Phi_0} = \left(\frac{2\pi n_0}{\lambda}\right)^2 J(\sigma, 0) \cdot \cos\theta. \quad (6)$$

Fig. 1 shows the height profile of one synthetic surface created with the above procedure ($\delta_e = 0.04$ nm, $L_e = 2000$ nm, $\delta_g = 1.33$ nm, $L_g = 2$ nm).

Fig. 2 presents a simulated scattering function of this surface, illuminated at normal incidence by a monochromatic light beam ($\lambda = 847$ nm). The detector is located within the plane of incidence, and is characterized by a field of view of 1°. This field of view is simulated by an angular average on the scattering function.

This simulated function can be used to evaluate the roughness of the sample in the spatial pulsation range $[0, \frac{2\pi n_0}{\lambda}]$ by applying the classical relationship [14] between rms roughness $\delta$ and roughness spectrum $\gamma(\sigma)$

$$\delta^2 = 2\pi \int_\sigma \sigma\gamma(\sigma)\, d\sigma. \quad (7)$$

For the synthetic surface shown in Fig. 1, this method gives a rms roughness of 0.865 nm. This value is lower than that defined by the filter used for generating the surface, i.e.

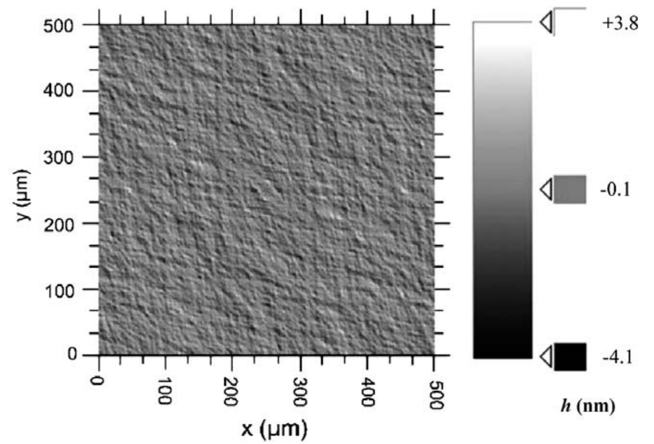


**Fig. 1.** Synthetic low-roughness surface model (greyscale representation).

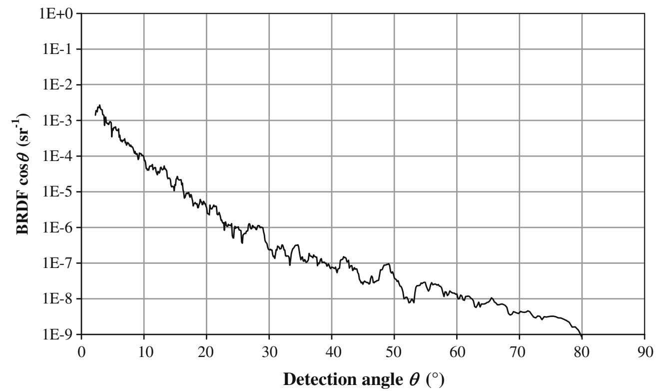


**Fig. 2.** Cosine-corrected BRDF of a synthetic 500 × 500 µm² low-roughness surface (light beam incident angle $i = 0°$, $\lambda = 847$ nm, detector in the plane of incidence, field of view 1°).

$$\delta = \sqrt{\delta_g^2 + \delta_e^2} \approx 1.33\,\mathrm{nm} \quad (8)$$

since the integration (7) is performed in the restricted range $[0, \frac{2\pi n_0}{\lambda}]$.

Let us now add to this surface some isolated, dome-shaped defects with diameters between 3 and 8 µm, heights lower than 0.2 µm, and the same refractive index as the surface. Fig. 3 shows the location and the size of these defects. The left-hand surface (a) has 10 defects, while the right-hand surface (b) has 60. The lower panel shows the computed scattering functions of both new surfaces as well as the original.

Notice that 60 defects increase the overall level of the cosine-corrected BRDF by a substantial factor. (From 100 to 1000, increasing with the scattering angle.) The impact of only 10 defects is less pronounced (the factor ranges between 1.5 and 10, and doesn't appear related to angle), but clearly cannot be neglected. Determination of the rms roughness through an ARS measurement has become inaccurate in both cases due to the presence of a few localized defects (the computation leads to a rms roughness of 22.6 nm for the surface including 60 isolated defects, 3.9 nm for the surface including only 10 defects, to be compared to 0.865 nm for the surface without isolated defects).

To overcome this problem, the first step is to reduce the number of defects in the illuminated area. (Recall that this cannot always be achieved by cleaning or repolishing the sample.) The only solution is to decrease the dimensions of the illuminated area.

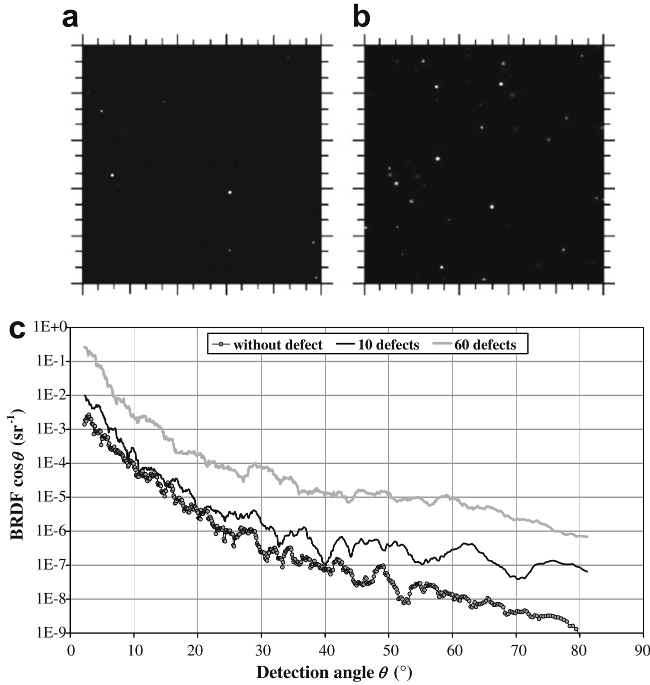


**Fig. 3.** Influence of localized defects (diameter between 3 and 8 μm, height less than 0.2 μm) on light scattering from a $500 \times 500\ \mu m^2$ synthetic low-roughness surface (see Fig. 1). (a) The surface with 10 defects. (b) The surface with 60 defects. (c) Cosine-corrected BRDFs.

Let us divide the synthetic surface into smaller squares, each with a surface area 100 times smaller (i.e., $50 \times 50\ \mu m^2$). The probability of having two defects in the region is greatly reduced, and may become negligible if the total number of defects remains small. Two different cases then have to be analyzed: either the surface element is free of defects (in which case the observed scattering function is representative of intrinsic roughness), or it includes only one defect. In the latter case, the scattering function will be greatly affected and instantly recognizable.

Fig. 4 shows that the computed scattering function of a smaller zero-defect region is close to that obtained for the whole $500 \times 500\ \mu m^2$ synthetic surface. We stress that decreasing the illuminated surface area greatly reduces the number of height profile points used in the computation. As a consequence, the angular sampling pitch is significantly increased and becomes close to 1° (grey circles in Fig. 4). Nevertheless, using this curve to compute

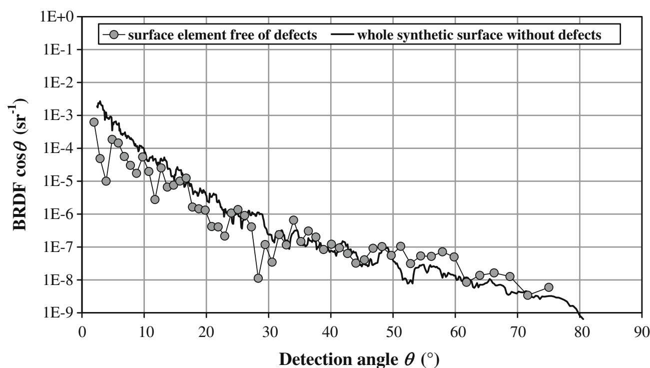


**Fig. 4.** The computed scattering functions of two different configurations: a defect-free $50 \times 50\ \mu m^2$ region (grey circles) and the full $500 \times 500\ \mu m^2$ synthetic surface with no defects (thick black line).

the rms roughness of the smaller region yields $\delta = 0.855$ nm, very close to that determined for the whole surface in the same pulsation range, $\delta = 0.865$ nm. We can perform the same computation for the other defect-free surface elements. Fig. 5 summarizes these results, the horizontal black line corresponding to their average, which is obviously identical to the rms roughness of the whole defect-free surface.

If the $50 \times 50\ \mu m^2$ synthetic surface element includes a defect, its scattering function will be affected. Detailed studies of this phenomenon have been performed for instance by Germer et al. [20], in close connection with the optimization and high-accuracy calibration of laser particle scanners [21,22]. It is important to stress that our objectives are different from theirs. First of all, we wish to identify all surface elements whose scattering functions indicate the presence of a defect, so that they may be removed from consideration when computing the intrinsic roughness of the surface. Second, we would like to determine the distribution of these surface elements and estimate the sizes of their defects. Hence, the purpose of our instrument is really quite different from that of a laser particle scanner. For this reason, we are justified in employing a simpler (nearly phenomenological) model for the scattering function of regions with an isolated defect.

Fig. 6 shows the computed scattering function that results when a small cylinder (2.3 μm in diameter, 0.1 μm in height) is placed on a $50 \times 50\ \mu m^2$ surface element.

The shape of this scattering function closely approximates an Airy pattern, corresponding to diffraction by a circular stop of diameter $2a$ [15]:

$$\mathrm{BRDF} \cdot \cos\theta \propto \left[\frac{J_1\left(\frac{2\pi a}{\lambda}\sin\theta\right)}{\frac{2\pi a}{\lambda}\sin\theta}\right]^2. \tag{9}$$

In the case of a single defect with diameter greater than the diffraction limit (i.e., $1.22\lambda$), the scattering function will present one or more oscillations. Its minima occur at specific scattering angles $\theta_m$ given approximately by

$$\sin\theta_m \approx \frac{Z_m}{\pi} \cdot \frac{\lambda}{2a}, \tag{10}$$

where the $Z_m$ are zeros of the $J_1$ Bessel's function (3.8317, 7.0156, 10.1735, and so on).

To comprehensively characterize the roughness properties of a sample, we need to record the scattering function of each small surface element. If we consider a standard 1" – diameter optical substrate, for example, and wish to characterize at least 80% of its surface, then approximately $M = 160,000$ $50 \times 50\ \mu m^2$ surface elements will need to be scanned. This number is quite large, especially if we keep in mind that each cosine-corrected BRDF function requires from 20 to 100 angular positions ($K$).

### *2.2. Rapid measurement of scattering functions*

To rapidly record so many data points ($M \times K$ is about 10 million) while maintaining a reasonable signal-to-noise ratio, some sort of multiplexed acquisition scheme is required. Two solutions can be imagined: either a photodiode array is employed to sample the whole angular range (angular multiplexing), or the optical surface under testing must be imaged in the focal plane of a CCD camera (spatial multiplexing).

Many systems based on CCD arrays have been proposed in the field of computer vision and graphics, where the rapid determination of surface texture is considered an interesting problem. In this context, BRDF data are then used to render an object's appearance. Both angular [23–26] and spatial [27–29] multiplexing schemes

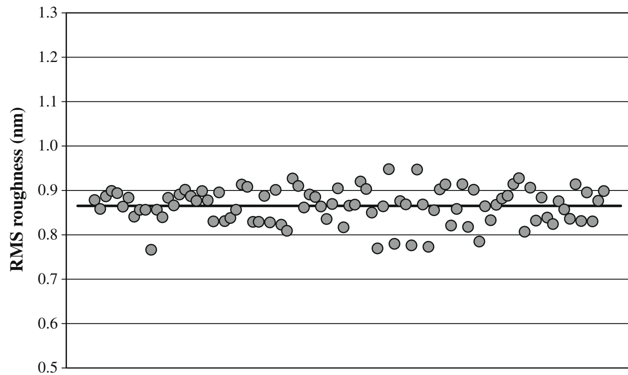


**Fig. 5.** RMS roughnesses of defect-free $50 \times 50\ \mu m^2$ surface elements (black line: average of the results).

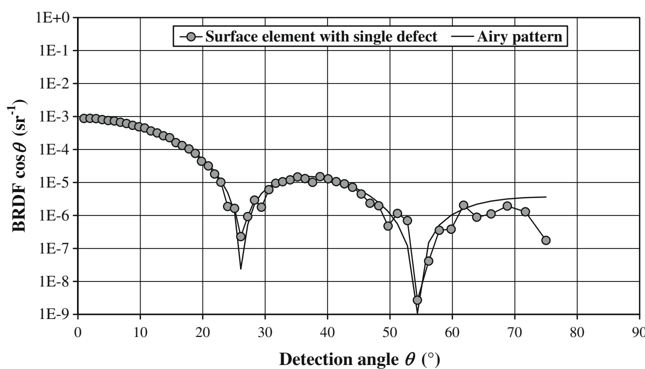


**Fig. 6.** Computed scattering function for a $50 \times 50\ \mu m^2$, low-roughness surface element with a 2.3 μm-diameter isolated defect. The black line is an Airy pattern.

have been investigated, but the optical scattering instruments used in this field are always adapted to very rough surfaces.

An optical scattering instrument based on angular multiplexing was proposed in 2000 by Rothe et al. [30]. The latest version of their instrument [31] consists of a catadioptric system: an elliptical mirror maps half of a hemispheric field of view onto a commercially available CMOS sensor ($656 \times 491$ pixels). This system provides up to 53 BRDFs per second. Spot sizes as low as $20 \times 40\ \mu m^2$ are reported for visible wavelengths, resulting in efficient particle detection [32]. Under this kind of scheme, comprehensive characterization of a one-inch sample surface (i.e., 160,000 BRDFs) would require about 1 h for the shortest reasonable integration time $\tau$ (typically 20 ms).

This is one of the reasons we prefer the CCD spatial multiplexing scheme, which permits sampling of all surface coordinates simultaneously. In this way we can dramatically increase the integration time (up to 1 min) while limiting the characterization process to a similar duration $T$ ($T = K\tau$ for spatial multiplexing). Under a classical goniometric light scattering arrangement we could imagine replacing the CCD array with a scanning laser spot, but in this case a similar scan duration (for instance, 1 min) would imply a much greater bandwidth $B$. ($B$ would be larger than $M/2\tau$, which is 1.5 kHz.) This would be necessary to ensure accurate sampling of the large dynamic range and rapidly varying scattering signals associated with defects. And obviously, this bandwidth increase will degrade the signal-to-noise ratio of the scattered light measurements. The CCD approach therefore seems preferable, as long as we can guarantee stable relative positioning between the sample surface and the photodiodes of the array during the BRDF recording.

## 3. Description of the CCD-ARS instrument

In 1976, J.E. Harvey described scattering as a linear, shift-invariant process [33,34]. In the latter reference, Harvey presents scattered light profiles recorded between −90° and +90° for various angles of incidence on polished and aluminized quartz substrates. He then demonstrates that all the curves become identical if they are represented in "direction cosine" space, i.e., expressed as a function of $(\sin\theta - \sin i)$. As usual, $\theta$ is the angle of detection; $i$ is the angle of incidence.

In accordance with the theoretical works on the reciprocity principle published by Greffet [35] and Snyder [36], we propose to extend the Harvey's approach by fixing the detection arm ($\theta = 0$). The lighting arm becomes mobile instead, so that $i$ can vary between a few degrees and 90°. This choice leads to a new arrangement in which the position and orientation of the sample are constant relative to the detector. The sample is thus easily imaged on a photodiode array. Moreover, we use a back-illuminated, scientific-grade CCD as the detector. This device samples about one million elementary pixels and is capable of reaching ultra-low BRDF levels thanks to the large integration time (up to 1 min), enabled by the negligible dark current level. A schematic of the CCD-ARS instrument is given in Fig. 7.

The light source is a high-power (15 mW) Super Luminescent Diode (SLD) centered at 840 nm, manufactured by Superlum [37]. Its spectral bandwidth ($\Delta\lambda = 50$ nm) is large enough to cancel the far-field speckle typical of coherent laser lighting, yet quite similar to the monochromatic configuration assumed by our numerical simulations. The first fiber link is a standard single-mode fiber (Corning Puremode HI-780), while the second is an all-silica, step index multimode fiber with core diameter $2a = 600\ \mu m$ and numerical aperture $\sin\theta = 0.25$. The two links (transmission $T_f$ about 92% for each) are coupled via a pair of identical objectives (transmission $T_1$ about 85%). A motorized filter wheel occupies the intervening space, to select an optical density (0, 2 or 4). The lighting objective is telecentric (with the same transmission $T_1$) and provides a magnified image (the magnification $M$ is about 19) of the multimode fiber's extremity, which is located in its focal plane (see [38] for a more detailed description of this device). The lighting system is installed on a mechanical arm that rotates (by angle $i$) around the sample. (The axis of this rotation is vertical, and lies in the front face of the sample.) The area illuminated by the beam is an ellipse with an 11.4 mm minor axis ($2aM = 0.6\ \text{mm} \times 19 = 11.4$ mm) and an $(11.4/\cos i)$ mm major axis, where $i$ is the incidence angle of the beam. The half divergence of this lighting beam is about 0.75° ($\sin\theta/M = 0.25/19 = 0.013$ rad).

The surface of the sample is imaged by a Princeton Instruments PIXIS 1024B camera [39], which uses a back-illuminated, scientific-grade CCD with a $1024 \times 1024$ imaging array and 100% fill factor (square pixels, with side $p = 13\ \mu m$). At the SLD's central wavelength, the quantum efficiency $\eta$ of the CCD is about 60%. The camera can be maintained at −70°C by means of an interior thermoelectric cooler; at this temperature, the dark current is limited to 0.001 $e^-$/pixel/s. The single-pixel full well figure is around 120 $ke^-$. Read-out and digitization of the CCD data are performed at 100 kHz on 16 bits (read noise 4.3 $e^-$ rms).

The imaging objective is an MVO TM$^{TM}$Telecentric Lens from Edmund Optics, Ref. NT55-349 [40] with transmission $T_2 = 55\%$, magnification $G = 0.25$, a working distance of 160 mm, and a nominal aperture number of 6 ($N$). We stress that the telecentric objective is a key element defining the characteristics of our instrument. In a telecentric objective the entrance pupil is rejected at infinity, which guarantees that the angular coordinates of the chief ray defining the direction of scattered light are the same at all points on the sample surface. This property is illustrated in Fig. 8.

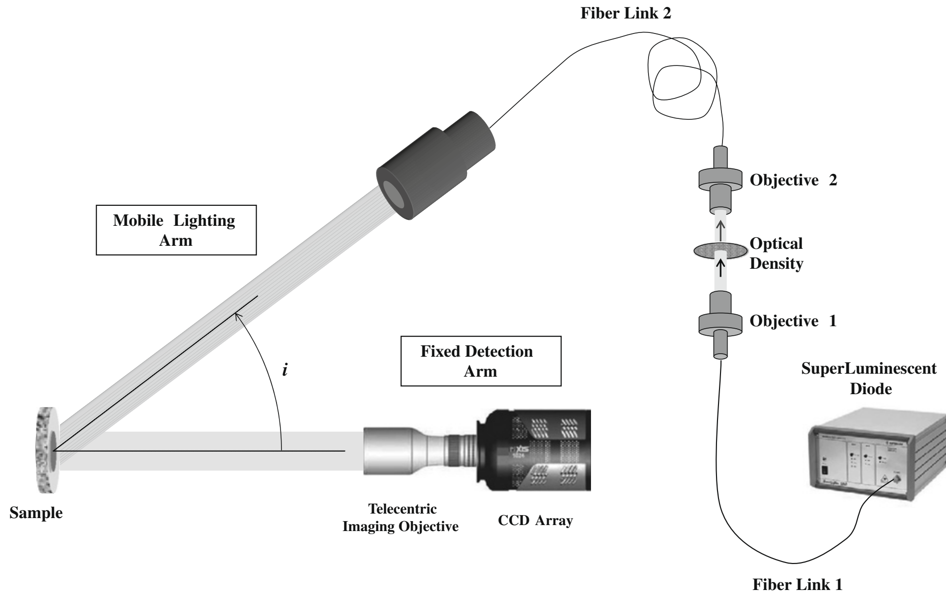


**Fig. 7.** The CCD-ARS instrument.

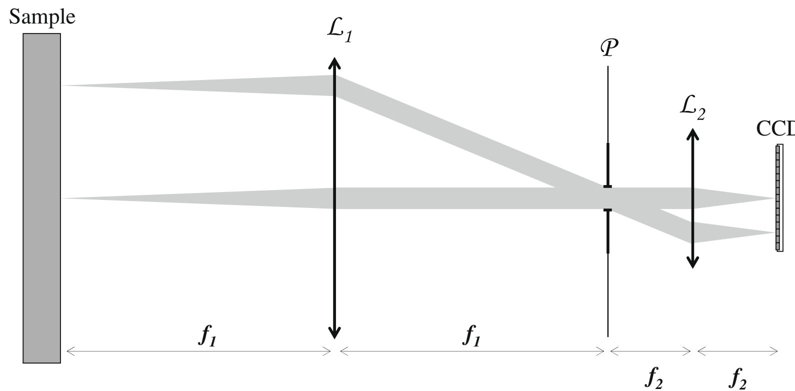


**Fig. 8.** The working principle of a telecentric objective used as an imaging device.

An aperture stop is placed in the common focal plane of lenses $L_1$ and $L_2$, which are used to simulate the telecentric objective. The entrance pupil and exit pupil are located at infinity, so the chief ray is horizontal in both sample space and CCD space for any pixel of the detector array. The field of view of the detector can be controlled by adjusting the diameter of the aperture stop. The magnification factor $G$ is determined by the focal lengths of the two lenses ($G = f_2/f_1$). The half-divergence $\alpha$ of a scattered beam entering the pupil of the imaging objective is about 1.2° ($\tan\alpha = G/2N = 0.021$). Moreover, the area imaged by the CCD camera is $1024\,p/G = 53.2$ mm square. As indicated previously this telecentric configuration is also implemented in the lighting system, which guarantees that the angular coordinates of the beam are identical for all points on the surface of the sample [38].

The apparatus we describe is in some ways similar to that proposed by Boulbry et al. in 2006 [41] for imaging skin lesions. Aside from the fact that our aims are completely different, we introduce two major changes. First, rather than 16 LED illumination tubes distributed one a hemisphere, our experiment uses just one tightly collimated and highly uniform beam mounted on a motorized rotating arm. This makes it possible to adjust features of the angular scan, especially pitch, in accordance with the divergence of the beam and the scattering properties of the surface. Second, we use a high $F$-number telecentric objective to transform the CCD images into BRDF recordings. Small square areas of the sample are easily defined in terms of image pixels. It is thanks to these two changes that our experiment provides accurate light scattering measurements instead of simple surface imaging.

## 4. Measurement range and detection limit

Suppose that the sample is a perfect diffuser. The number $N_s$ of photoelectrons accumulated in a single pixel for an incidence angle close to zero is defined by the following equation:

$$N_s = T_1^3 T_f^2 10^{-OD} \frac{P_s \tau}{\pi (Ma)^2} \cdot \frac{T_2}{1 + 4N^2} p^2 \frac{\eta\lambda}{hc} \rho, \tag{11}$$

where $T_1$ is the common transmission of our 3 relay objectives, $T_f$ is the transmission of one fiber link, $OD$ is the optical density of the filter in the path of the beam, $P_s$ is the optical power delivered by the source, $M$ is the magnification ratio of the lighting objective, and $2a$ is the core diameter of the multimode fiber. The factors $G, N$ and $T_2$ are the magnification factor, aperture number, and

transmission of the telecentric objective respectively. Finally, $\tau$ is the integration time of the CCD array, $\eta$ is its quantum efficiency at the central wavelength $\lambda$ of the source, $p$ is the lateral dimension of a CCD pixel, and $\rho$ is the albedo of a perfect diffuser.

By substituting in the appropriate numerical values for our device, we obtain the compact relation

$$N_s = 1.26\,10^8 \times 10^{-OD}\tau\rho. \tag{12}$$

The camera's internal shutter provides integration times $\tau$ no shorter than 80 ms. Even at this limit, an optical density of 2 is required to avoid saturating the pixels. For a perfect diffuser ($\rho = 1$), the mean number of photo-electrons accumulated in a single well is about 100,800. While the pixels are not saturated, this intensity still requires a (software-selectable) gain of 2 $e^-$/count to maintain digitized data within the 16-bit range.

Three noise sources have to be considered: photon noise, shot noise associated with the dark current, and the overall read-out noise of the camera $N_R$. We can write

$$\sigma_T = \sqrt{N_s + D\tau + N_R^2}, \tag{13}$$

where $D$ is the dark current of the CCD and $\tau$ is the integration time. In the case of a perfect diffuser, the overall rms noise level can be estimated at 317 electrons (photon noise is obviously dominant).

To estimate the smallest BRDF that can be measured with such a device, we first have to define a maximum reasonable integration time. We propose the 1-min duration mentioned in Section 2. Even with so large an integration time, the dark current contribution remains negligible (less than 0.1 $e^-$). The uncertainty is now dominated by the camera's read-out noise. The BRDF value corresponding to our detection limit (a signal-to-noise ratio of 2) is then about $10^{-9}$ $sr^{-1}$.

## 5. Experimental results

### 5.1. Perfect diffuser

The characterization of a perfect diffuser is necessary to calibrate our CCD-ARS instrument. Fig. 9 shows a sequence of images recorded by the CCD array for incidence angles between 20° and 90°, when the sample is a LABSPHERE Spectralon Reflectance Standard [42] with hemispherical reflectance factor equal to 0.99 around 840 nm.

As previously mentioned, the illuminated area is an ellipse whose major axis is inversely proportional to $\cos i$. The intensity of the scattered light clearly decreases as the incidence angle increases. The smallest lighting angle achievable is 20° due to the dimensions of the two objectives. Obviously, the instrument can be calibrated only for those pixels which are continuously lit over the entire angular scan (i.e., those illuminated in the first image).

Fig. 10 shows the scattered light intensity recorded during this angular scan for one such pixel, selected at random. The data are well fit by the theoretical response of a perfect diffuser

$$N_s(i) = N_{\max}\cos i, \tag{14}$$

where the normalization parameter $N_{\max}$ was adjusted by a least-squares method.

For all pixels inside the initially illuminated area, we obtain a similar level of agreement. This result confirms the validity of our measurement method. Fig. 11 shows the values obtained for this calibration constant ($N_{\max}$) for each CCD pixel inside a 6.5 mm square. The slight variations are due to the imperfect uniformity of the beam, but this effect can now be canceled out across the whole image.

In Fig. 9, we also note the presence of a bright edge to the right of the last few images. This parasitic light is due to grazing reflection from the sample edge. While this pattern is obviously located well outside of the measurement area, its effect on the background

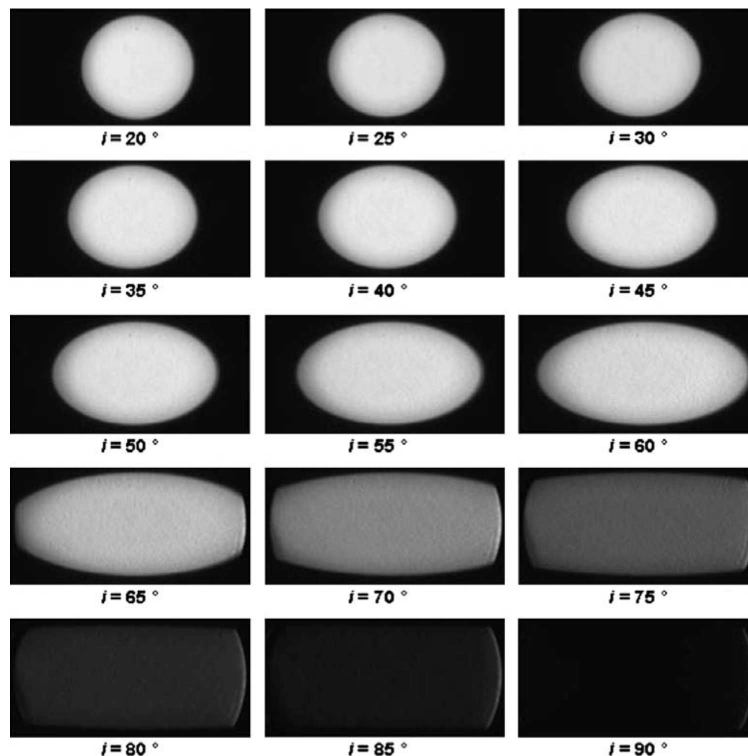


**Fig. 9.** CCD images recorded with a perfect diffuser.

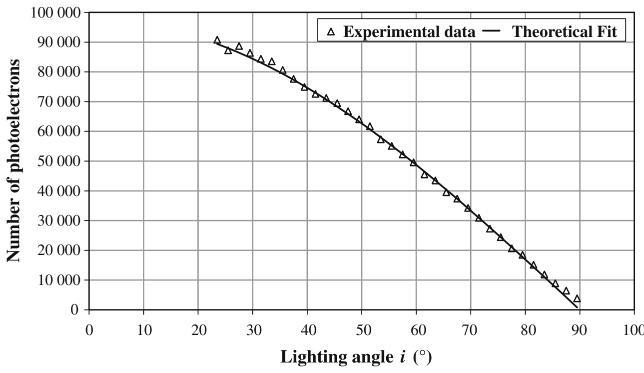


**Fig. 10.** The number of photoelectrons accumulated by a single CCD pixel as a function of lighting incidence angle (triangles: experimental data; black line: cosine fit).

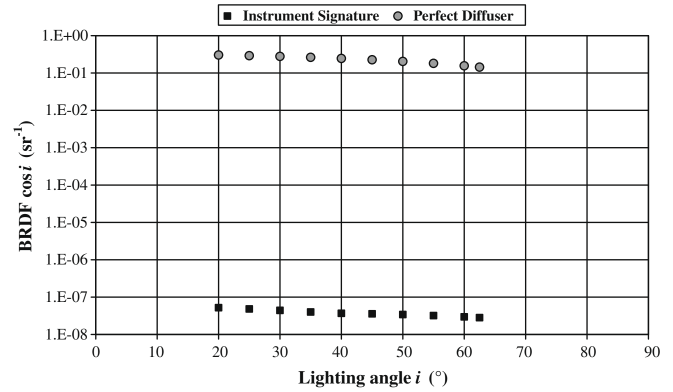


**Fig. 12.** CCD-ARS instrument signature for lighting angles between 20° and 65° (black squares). The scattering intensities of a perfect diffuser are plotted as grey circles.

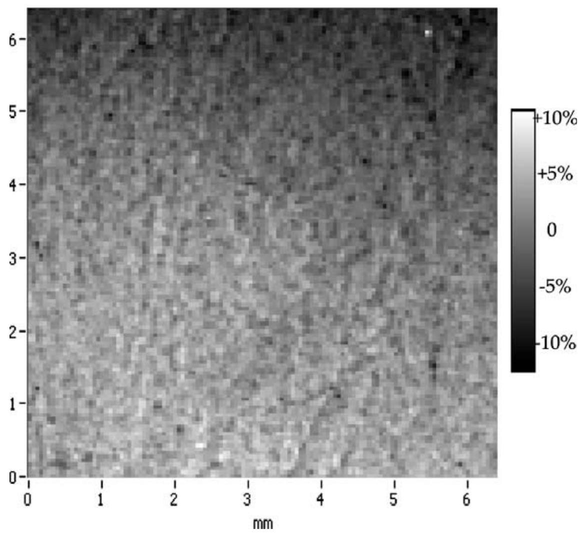


**Fig. 11.** Relative variation of the calibration constant $N_{max}$ (maximum number of photoelectrons recorded with a perfect diffuser) at each pixel position within a 6.5 mm square.

level can be troubling for low-roughness samples at incidence angles above 65°. The shape and structure of the sample itself should be carefully chosen to minimize this effect. We will return to this point in Section 6.

### 5.2. Instrument signature measurement

As defined by the American Society for Testing and Materials (ASTM), a *signature measurement* is the lowest level of BRDF measurable with a given instrument [43]. As recalled by Asmail [8], our signature is equivalent to the BRDF of an ideal, scatter-free sample due to instrument limitations. In our case, the signature was determined by removing the sample and otherwise measuring the effective BRDF under the same conditions (range of angles, optical density, integration time) that would later be used in actual sample measurements (see Section 5.3). Accordingly, the incident angle varied between 20° and 65°, the optical density was set to zero, and the integration time was 100 s. The equivalent BRDF level varied from $5 \times 10^{-8}$ sr$^{-1}$ at 20° to $3 \times 10^{-8}$ sr$^{-1}$ at about 60°. The rms noise under these conditions is about $2 \times 10^{-9}$ sr$^{-1}$. The instrument signature is therefore dominated by stray light and Rayleigh's scattering. Fig. 12 compares the result of this measurement to that achieved on a perfect diffuser.

### 5.3. Silicon wafer

To complete our evaluation of the CCD-ARS instrument and demonstrate its efficiency at locating isolated defects, we examine a low-roughness silicon wafer with some surface particles (due to imperfect cleaning). The central part of the CCD image (at a lighting angle of 20°), corresponding roughly to the illuminated area, is shown in Fig. 13a. The intensity of the lighting beam is maximal

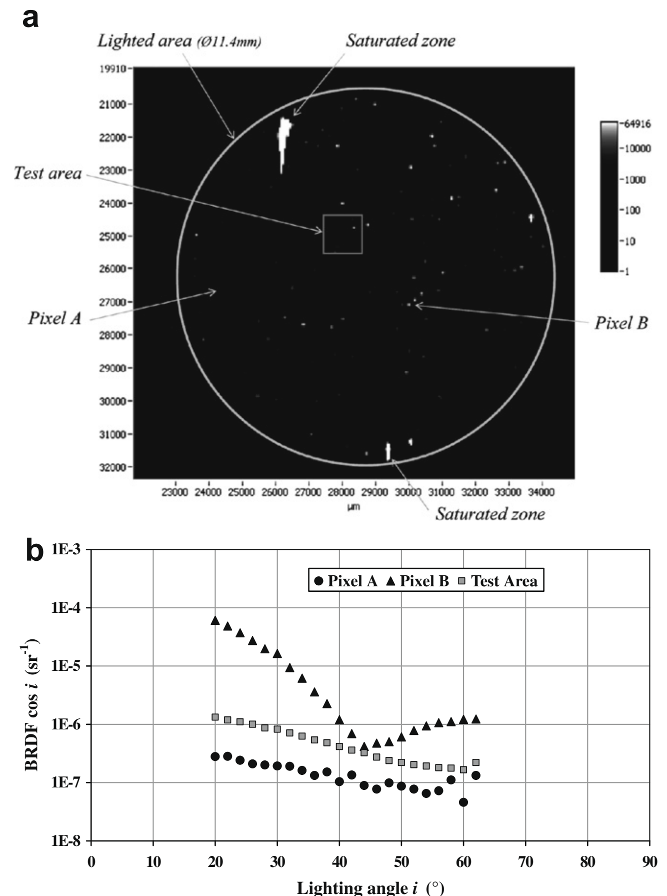


**Fig. 13.** (a) A low-roughness silicon wafer imaged with the CCD-ARS instrument (the lighting angle is 20°). (b) Cosine-corrected BRDFs of selected pixels (black circles: pixel A, without a defect; black triangles: Pixel B, with a single defect; grey squares: a 1 mm square test area).

(zero optical density) and the integration time is 15 s. In the saturated zones (solid white) excess photo-electrons flow over to surrounding pixels, usually in the same column. Obviously, the BRDF measurement can not be achieved in these regions of the CCD array.

The pixel labeled A on Fig. 13a is associated with a surface element which is clearly free of particles. The BRDF of this surface element, shown in Fig. 13b, is a gradually decreasing function of angle. Its mean level is about $10^{-7}$ sr$^{-1}$, which is 5 times greater than the instrument signature.

In contrast, the pixel labeled B on Fig. 13a is associated with a surface element containing one foreign particle. The shape of the BRDF is comparable to the theoretical result presented in Fig. 6, and clearly characteristic of diffraction from a small stop. The position of the minimum ($i_1 = 44°$) indicates that the diameter $2a$ of this particle is about 1.5 μm, since from (10) we can write

$$2a \approx \frac{3.832}{\pi} \cdot \frac{\lambda}{\sin i_1}. \quad (15)$$

According to the same expression (10), the smallest particles which can be identified by this method will have a diameter of about 1 μm. We note that each pixel of our camera is about 13 μm square, which means that the sample area observed by one CCD pixel is equal to 52 μm (the magnification of the telecentric objective is 0.25). These data therefore prove that our CCD-ARS instrument is capable of detecting extremely small structures, with lateral sizes 50 times smaller than the elementary area. This resolution is clearly an outstanding feature of our instrument.

Finally, we measured scattered light within a larger test area 1 mm square (shown by the grey line on Fig. 13a). This region, containing 400 elementary pixels and a few foreign particles, is similar to the numerical simulations presented in Section 2. An enlarged view of this test area is shown in Fig. 14a, on an inverted 16-bit logarithmic scale.

Depending on the pixel selected, the recorded BRDFs (see Fig. 14b) resemble either pixel A (no oscillations, level close to $10^{-7}$ sr$^{-1}$) or pixel B (oscillating shape, level varying between a few $10^{-6}$ and $10^{-4}$sr$^{-1}$). The global BRDF of this region (grey squares in Fig. 13b) obtained by averaging over all pixels, however, does not exhibit any oscillations whatsoever. It is also characterized by a scattering level about 4 times higher than the intrinsic response of the surface would indicate. This result is in perfect accordance with the numerical simulations presented in Section 2 (see especially Fig. 3). It also illustrates the kind of erroneous information that can be produced by classical BRDF instruments when the surface topology includes localized defects [15,44].

It is important to stress that the Point Spread Function (PSF) of the telecentric objective has been adapted to the pixel size of the CCD array. Indeed, the diameter $D$ of the first ring of the PSF is given by $D = 2.44N\lambda$, where $\lambda$ (840 nm) is the central wavelength of the source and $N$ is the aperture number of the telecentric objective ($N = 6$). The resulting diameter $D$ is 12.3 μm, slightly less than

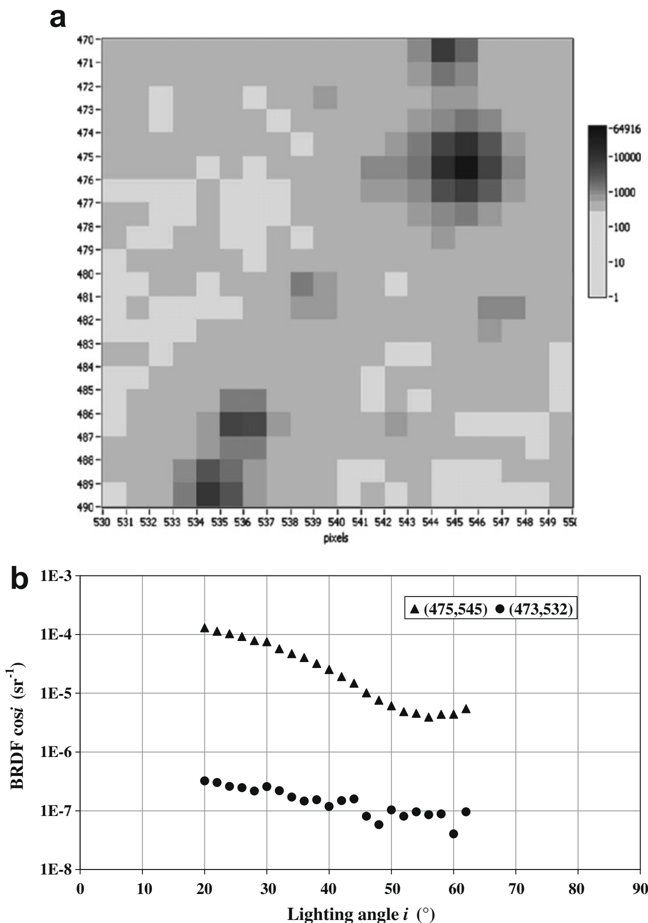


**Fig. 14.** Enlarged view of the 1 mm square test area. (a) The CCD image recorded for a lighting angle of 20° (inverted logarithmic scale). (b) Two cosine-corrected BRDFs. Black triangles: pixel (475,535); black circles: Pixel (473,532).

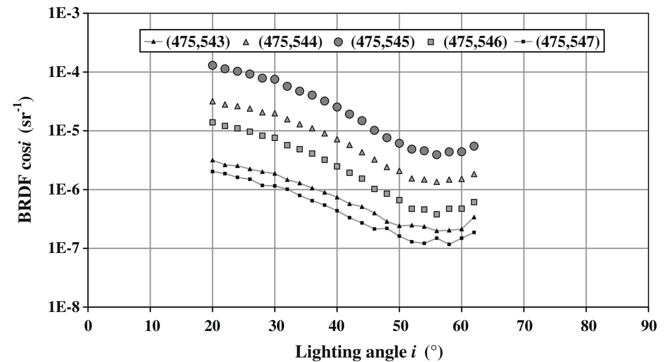


**Fig. 15.** Cosine-corrected BRDFs for pixels in the vicinity of a localized defect.

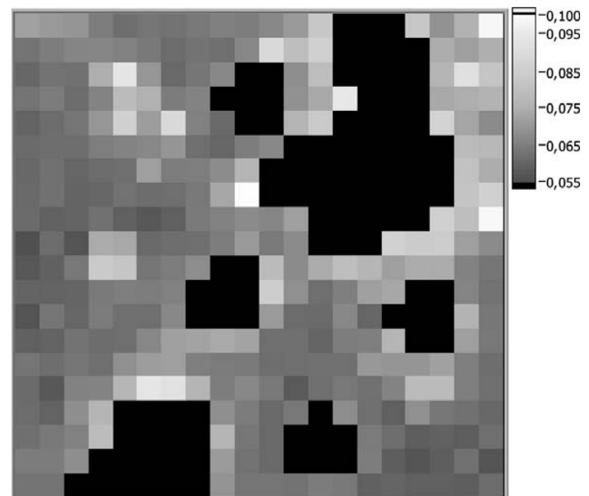

**Fig. 16.** RMS roughness map of the 1 mm square test area, after suppression of all pixels enhanced by a nearby defect (black pixels). The roughness is expressed in nm on a linear greyscale.

| Localized defects | Number | Level (a.u.) |
|---|---|---|
| Diameter ~ 1 μm | 4 | 130, 8, 1, and 1 |
| Diameter < 1 μm | 8 | 17,12, 2.5, 2, 2, 1, 1, and 1 |

| Intrinsic roughness | $\delta$ (nm) |
|---|---|
| Maximum value | 0.099 |
| Minimum value | 0.056 |
| Mean value | 0.068 |

**Fig. 17.** Detailed features detected in the 1 mm square test area.

the 13 μm pixel size. Nevertheless, the ratio between the peak of a particle-induced diffraction pattern and the intrinsic response of the surrounding surface can be up to several hundreds. The zone of influence of a particle can therefore spread out over a larger region up to 5 pixels in diameter. This effect is clearly visible in the BRDF curves presented in Fig. 15, and corresponds to the elevated signal in pixels near the defect at line 475 and column 535 in Fig. 14a.

It is thus necessary to eliminate a large zone around each isolated defect if we are to determine the intrinsic scattering properties of the surface. Fig. 16 shows the result of such a filtering process, as well as a revised computation of the rms roughness for each remaining pixel (linear greyscale). The mean roughness is about 0.068 nm, significantly less than the value computed on the whole test area (0.089 nm).

To complete this data processing, we generate a table (see Fig. 17) reporting the number and sizes of all sample defects as well as the intrinsic roughness of the surface. The information provided by our CCD-ARS instrument is quite comprehensive.

## 6. Conclusion and perspectives

This paper has described a new CCD-ARS instrument for measuring the scattered light profile of a low-roughness surface, and has proved that it can provide comprehensive information on surface defects as well as measuring the correct intrinsic roughness. The number of useful data points acquired during a single scan using this device can easily reach several millions (for example, 35 angular positions times 40,000 fully lit pixels). The positions and sizes of defects can be determined from obvious features of the scattered light profile in each CCD pixel. This apparatus can therefore be used to efficiently compare and qualify optical coating deposition processes.

To further improve this method and extend its range of applications, some small changes can be made in our design. First, the angular range should be extended to smaller angles. Incidence angles as low as 5° can be achieved using a dedicated telecentric objective with a greater working distance. At the same time, increasing the magnification ratio of the objective (to 0.5 instead of 0.25) would improve our spatial resolution at the sample surface (to 26 μm instead of 52 μm). The second improvement is also related to angular extension, but this time would extend the data to large angles (between 65° and 90°). The parasitic light observed in images at large incidence can be easily dealt with in at least two ways. By continuously morphing the beam, the shape of the illuminated region could be maintained during the angular scan. Alternatively, a dedicated sample holder could be created to support the new lighting strategy. Both improvements are currently in progress within our team [45].

Finally, the theoretical principles behind this roughness measurement method are clearly compatible with other spectral studies (wavelength switching of incoherent sources) and polarization analysis, as previously defined by our team on a standard ARS instrument [38,46].

## References

[1] J.M. Bennett, L. Mattsson, Introduction to Surface Roughness and Scattering, 2nd ed., OSA, Washington, DC, 1999.
[2] J.C. Stover, Optical Scattering: Measurement and Analysis, 2nd ed., Scatter Measurements and Instrumentation, SPIE, Bellingham WA, 1995 (Chapter 6).
[3] P. Roche, E. Pelletier, Appl. Opt. 23 (1984) 3561.
[4] C. Amra, C. Grezes-Besset, P. Roche, E. Pelletier, Appl. Opt. 28 (1989) 2723.
[5] C. Amra, D. Torricini, P. Roche, Appl. Opt. 32 (1993) 5462.
[6] T.F. Schiff, M.W. Knighton, D.J. Wilson, F.M. Cady, J.C. Stover, J.J. Butler, Proc. SPIE 1995 (1993) 121.
[7] J. Neubert, T. Seifert, N. Czarnetzki, T. Weigel, Proc. SPIE 2210 (1994) 543.
[8] C.C. Asmail, C.L. Cromer, J.E. Proctor, J.J. Hsia, Proc. SPIE 2260 (1994) 52.
[9] T.A. Germer, C.C. Asmail, Proc. SPIE 3141 (1997) 220.
[10] D.R. White, P. Saunders, S.J. Bonsey, J. van de Ven, H. Edgar, Appl. Opt. 37 (1998) 3450.
[11] T.A. Germer, C.C. Asmail, Rev. Sci. Instr. 70 (1999) 3688.
[12] A. Duparre, J. Ferre-Borrull, S. Gliech, G. Notni, R. Steinert, J.M. Bennett, Appl. Opt. 41 (2002) 154.
[13] S. Schröder, S. Gliech, A. Duparré, Appl. Opt. 44 (2005) 6093.
[14] C. Deumie, R. Richier, P. Dumas, C. Amra, Appl. Opt. 35 (1996) 5583.
[15] S. Maure, G. Albrand, C. Amra, Appl. Opt. 35 (1996) 5573.
[16] J.D. Rancourt, Optical Thin Films: User Handbook, SPIE, Washington, DC, 1996.
[17] C. Amra, C. Grezes-Besset, L. Bruel, Appl. Opt. 32 (1993) 5492.
[18] C. Amra, J. Opt. Soc. Am. A 10 (1993) 365.
[19] C. Amra, J. Opt. Soc. Am. A 11 (1994) 197.
[20] T.A. Germer, G.W. Mulholland, J.H. Kim, S.H. Ehrman, Proc. SPIE 4779 (2002) 60.
[21] C.A. Scheer, J.C. Stover, V.I. Ivakhnenko, Proc. SPIE 3275 (1998) 102.
[22] J.C. Stover, C.A. Scheer, Proc. SPIE 4449 (2001) 147.
[23] G.J. Ward, Comp. Graph. 26 (1992) 265.
[24] S.R. Marschner, S.H. Westin, E.P.F. Lafortune, K.E. Torrance, Appl. Opt. 39 (2000) 2592.
[25] K.J. Dana, Proc. ICCV 2001 2 (2001) 460.
[26] Y. Mukaigawa, K. Sumino, Y. Yagi, ProCams 2007, 4th IEEE International Workshop on Projector-Camera Systems, 2007.
[27] P. Debevec, T. Hawkins, C. Tchou, H.P. Duiker, W. Sarokin, M. Sagar, Proc. SIGGRAPH2000 (2000) 145.
[28] J.Y. Han, K. Perlin, ACM T. Graphic 22 (2003) 741.
[29] A. Wenger, A. Gardner, C. Tchou, J. Unger, T. Hawkins, P. Debevec, Proc. SIGGRAPH2005 (2005) 756.
[30] Th. Rinder, H. Rothe, A. Kasper, Proc. SPIE 4100 (2000) 136.
[31] C. Hahlweg, H. Rothe, Proc. SPIE 5965 (2005) 596519.
[32] Th. Rinder, H. Rothe, Proc. SPIE 4779 (2002) 72.
[33] J.E. Harvey, Proc. SPIE 107 (1977) 41.
[34] J.E. Harvey, Proc. SPIE 1165 (1989) 87.
[35] J.-J. Greffet, M. Nieto-Vesperinas, J. Opt. Soc. Am. A 15 (1998) 2735.
[36] W.C. Snyder, Appl. Opt. 41 (2002) 4307.
[37] <http://www.superlumdiodes.com/pdf/s840-b-i-20.pdf>.
[38] M. Lequime, L. Abel, C. Deumie, Proc. SPIE 5250 (2003) 271.
[39] <http://www.piacton.com/products/pixis/>.
[40] <http://www.edmundoptics.com/onlinecatalog>.
[41] B. Boulbry, T.A. Germer, J.C. Ramella-Roman, Proc. SPIE 6078 (2006) 60780R.
[42] <http://www.labsphere.com>.
[43] Standard Practice for Angle Resolved Optical Scatter Measurements on Specular or Diffuse Surfaces, ASTM E1392–E1396.
[44] M. Zerrad, C. Deumié, M. Lequime, C. Amra, Opt. Express 15 (2007) 9222.
[45] M. Zerrad, M. Lequime, C. Deumié, C. Amra, Invited Communication at Optical Fabrication, Testing and Metrology, SPIE 7102, Glasgow, 2008.
[46] O. Gilbert, C. Deumié, C. Amra, Opt. Express 13 (2005) 2403.